

Article

Thermocatalytic Performance of $\text{LaCo}_{1-x}\text{Ni}_x\text{O}_{3-\delta}$ Perovskites in the Degradation of Rhodamine B

Benjamin H. Christensen¹, Francesca Deganello², Valeria La Parola², Mads K. Jørgensen¹, Vittorio Boffa¹
and Martin B. Østergaard^{1,*}

¹ Center for Membrane Technology, Department of Chemistry and Bioscience, Aalborg University, DK-9220 Aalborg East, Denmark

² Istituto per lo Studio dei Materiali Nanostrutturati, Consiglio Nazionale delle Ricerche (CNR-ISMN), Via Ugo La Malfa 153, 90146 Palermo, Italy

* Correspondence: mbo@bio.aau.dk

Abstract: Perovskite-type $\text{LaCo}_{1-x}\text{Ni}_x\text{O}_{3-\delta}$ ($x = 0, 0.2, 0.4, 0.6,$ and 0.8) powders were synthesized by solution combustion synthesis. The crystal structure, morphology, texture, and surface were characterized by X-ray powder diffraction combined with Rietveld refinement, scanning electron microscopy, N_2 -adsorption, X-ray photoelectron spectroscopy, and zeta-potential analysis. The thermocatalytic properties of the perovskites were investigated by UV-Vis spectroscopy through degradation of rhodamine B in the temperature range 25–60 °C. For the first time, this perovskite system was proven to catalyze the degradation of a water pollutant, as the degradation of rhodamine B occurred within 60 min at 25 °C. It was found that undoped $\text{LaCoO}_{3-\delta}$ is the fastest to degrade rhodamine B, despite exhibiting the largest energy band gap (1.90 eV) and very small surface area ($3.31 \text{ m}^2 \text{ g}^{-1}$). Among the Ni-doped samples, the catalytic performance is balanced between two main contrasting factors, the positive effect of the increase in the surface area (maximum of $12.87 \text{ m}^2 \text{ g}^{-1}$ for 80 mol% Ni) and the negative effect of the Co(III) stabilization in the structure (78% in LaCoO_3 and 89–90% in the Ni-containing ones). Thus, the Co(II)/Co(III) redox couple is the key parameter in the dark ambient degradation of rhodamine B using cobaltite perovskites.

Keywords: perovskite; Rietveld refinement; energy band gap; thermocatalyst; catalytic degradation



Citation: Christensen, B.H.; Deganello, F.; La Parola, V.; Jørgensen, M.K.; Boffa, V.; Østergaard, M.B. Thermocatalytic Performance of $\text{LaCo}_{1-x}\text{Ni}_x\text{O}_{3-\delta}$ Perovskites in the Degradation of Rhodamine B. *Catalysts* **2023**, *13*, 325. <https://doi.org/10.3390/catal13020325>

Academic Editor: Pedro B. Tavares

Received: 9 January 2023

Revised: 23 January 2023

Accepted: 27 January 2023

Published: 1 February 2023



Copyright: © 2023 by the authors. Licensee MDPI, Basel, Switzerland. This article is an open access article distributed under the terms and conditions of the Creative Commons Attribution (CC BY) license (<https://creativecommons.org/licenses/by/4.0/>).

1. Introduction

Perovskite oxides are a class of metal oxide compounds with the general formula ABO_3 and similar structure to the original CaTiO_3 . The A-site is often occupied by alkaline earth or lanthanide metals, and the B-site by transition metals [1]. Their crystal structure and properties can be tailored by tuning the composition and synthesis route. Tanaka and Misono [2] have set up five main strategies for the optimization of the design of perovskites with catalytic properties: (1) select of the B-site, (2) control valency and vacancies by tuning A-site, (3) favor synergistic effects among B-site elements, (4) enhance the surface area, and (5) add precious metals. The ability of transition metals to change oxidation state makes B-site as the main catalytic site [3], and this can be greatly manipulated by changing the A-site or B-site composition [4,5].

The best overpotential values in oxygen reduction and oxygen evolution reactions were found for B-site cations with 3.5 or 7 d-electrons [6] and 1.3 e_g -electrons [7], and this makes lanthanum perovskites with either cobalt, nickel, or manganese at B-site interesting compositions. Lanthanum perovskites have been used in activation of peroxymonosulphate for degradation of organic pollutants [8–10]. Here, LaCoO_3 has been found to perform better than LaNiO_3 in decolorization of rhodamine B [8], while the LaNiO_3 has been found superior to LaMnO_3 , LaZnO_3 , and LaFeO_3 in degradation of ofloxacin [11]. This might be caused by the easiness of Ni and Co to change oxidation state [12]. In photocatalytic

degradation of rhodamine B, yttrium-cobalt-doped LaNiO_3 performs better than undoped LaNiO_3 [13].

The properties of perovskites can be tailored by controlling the energy band structure and oxygen vacancies that are both of importance in catalysis. The band gap can be tuned by processing and thereby enhancing purity of the crystal structures or by doping [14]. The doping of perovskites has shown to favor a minimum in band gap compared to their undoped counterparts [15]. Another study has shown that the band gap is not linearly correlated with the degree of doping [16]. Similarly, oxygen vacancies have been found to enhance the catalytic properties of LaCoO_3 in oxygen evolution reactions [17].

Developing catalysts that form reactive oxygen species (ROS) on their own, rather than splitting peroxy monosulphate or hydrogen peroxide as in Fenton-like processes, is of great interest, as this will reduce the amount of chemicals needed, and minimize hazardous substances. Perovskites such as $(\text{Ba}/\text{Ca}/\text{Mg})_{0.5}\text{Sr}_{0.5}\text{CoO}_3$ [18], $\text{Ca}_{0.5}\text{Sr}_{0.5}\text{NiO}_{3-\delta}$ [19], $\text{Sr}_{0.9}\text{Ce}_{0.1}\text{CoO}_3/\text{SrCoO}_{2.77}$ [20], $\text{Sr}_{0.85}\text{Ce}_{0.15}\text{FeO}_{3-\delta}$ [21], $\text{La}_x\text{Sr}_{1-x}\text{CoO}_{3-\delta}$ [22], and $\text{LaNiO}_{3-\delta}$ [23] have been found to be able to degrade organic pollutant dissolved in water under dark ambient conditions via a thermocatalytic process [24]. Among organic pollutants, rhodamine B is an interesting model pollutant. It is a dye used in the textile industry [25], and if not removed, it represents an environmental and health issue. For example, rhodamine B is mutagenic and carcinogenic [26], and it is of utmost importance to remove from wastewaters to avoid pollution of receiving waters.

In this study, a systematic investigation of the effect of Ni in $\text{LaCo}_{1-x}\text{Ni}_x\text{O}_{3-\delta}$ perovskites was carried out. These chemical compositions were chosen since mixed Co-Ni oxides have been found to exceed the catalytic activity of the pure metal oxides in other systems [27,28]. The perovskites were synthesized through solution combustion synthesis using citric acid as a fuel [29]. Due to the difficulty in producing LaNiO_3 using solution combustion synthesis, this end member was not part of the study, as it contained byproducts, such as the La_2NiO_4 spinel phase and NiO phase [30]. In fact, LaNiO_3 can be prepared using high oxygen pressure during calcination [31,32]. The calcined perovskite oxide powders were characterized for their structural differences in the bulk and surface using X-ray diffraction and X-ray photoelectron spectroscopy, respectively. Their surface charge was determined by zeta-potential measurements, their energy band gap was determined from diffuse reflectance spectra, and their textural properties were investigated by N_2 -adsorption with Brunauer–Emmett–Teller methodology. Finally, their morphology was observed by Scanning Electron Microscopy and their catalytic activity was evaluated through the thermocatalytic degradation of rhodamine B under dark conditions using UV–Vis detection.

2. Results

2.1. Structural and Compositional Characterization

The structure of the synthesized perovskites after calcination at 1000 °C was determined by XRD. The XRD patterns are shown in Figure 1, including a graphical Rietveld refinement performed to investigate the impact of nickel addition on the lattice parameters, crystallite size, and microstrain of $\text{LaCoO}_{3-\delta}$ -based perovskites. The Rietveld results are summarized in Table S1. All perovskites showed the rhombohedral structure as previously shown for LaCoO_3 [33], and Ni-doped LaCoO_3 perovskites [34,35]. As previously noted, the LaNiO_3 perovskite could not be synthesized as single-phase under the given conditions even though both pH and reducers-to-oxidizers ratio were changed. As LaNiO_3 was previously obtained by calcination under oxygen pressure [31,32], it is assumed that the smaller amount of oxygen in normal atmosphere favors the formation of Ni^{2+} . The diffractogram of $\text{LaNiO}_{3-\delta}$ is reported in Supplementary Materials (Figure S1) showing the formation of three different phases, namely LaNiO_3 , NiO, and La_2NiO_4 . Considering the Co-containing perovskites, the Ni-rich compositions, 60 and 80 mol% Ni, have minor percentage of NiO as secondary phase, below 1 wt%. We suppose that this low amount of NiO, which does not have thermocatalytic properties itself, cannot have any important

influence on the thermocatalytic performance of the Ni-rich samples. The cell volume of the perovskites increases for all samples with increasing Ni content due to the larger size of Ni-ions compared to Co-ions [36], however, the volume is constant in the nickelate area (Figure 2a). This is based on the assumption that both cobalt and nickel are mainly in low spin states, as previously reported [35]. However, the unit cell parameters change differently in the cobaltite and nickelate compositions. The a/b parameter increases with Ni-content in the cobaltite area and decreases with Co-content in the nickelate composition (Figure 2b). Thus, it could be suggested that the increasing Ni-content overall ensured a larger parameter, although the a/b ratio is slightly lower in the nickelate range compared to the cobaltite range. The c-parameter (Figure 2b) seems to reach a maximum around 50 mol% doping as it increases with doping of both Ni and Co in the cobaltite and nickelate range, respectively. The microstrain (Figure 2c) shows a similar trend as the c-parameter. The crystallite size decreases with increasing nickel doping (Figure 2d) in agreement with a previous study [37]. Here, we find a significant change in crystal size when changing from Ni-doped cobaltite to Co-doped nickelate. The comparison of atomic coordinates of $\text{LaCoO}_{3-\delta}$ and $\text{LaCo}_{0.2}\text{Ni}_{0.8}\text{O}_{3-\delta}$ from the Rietveld refinement and the ICDD database is found in Table S2.

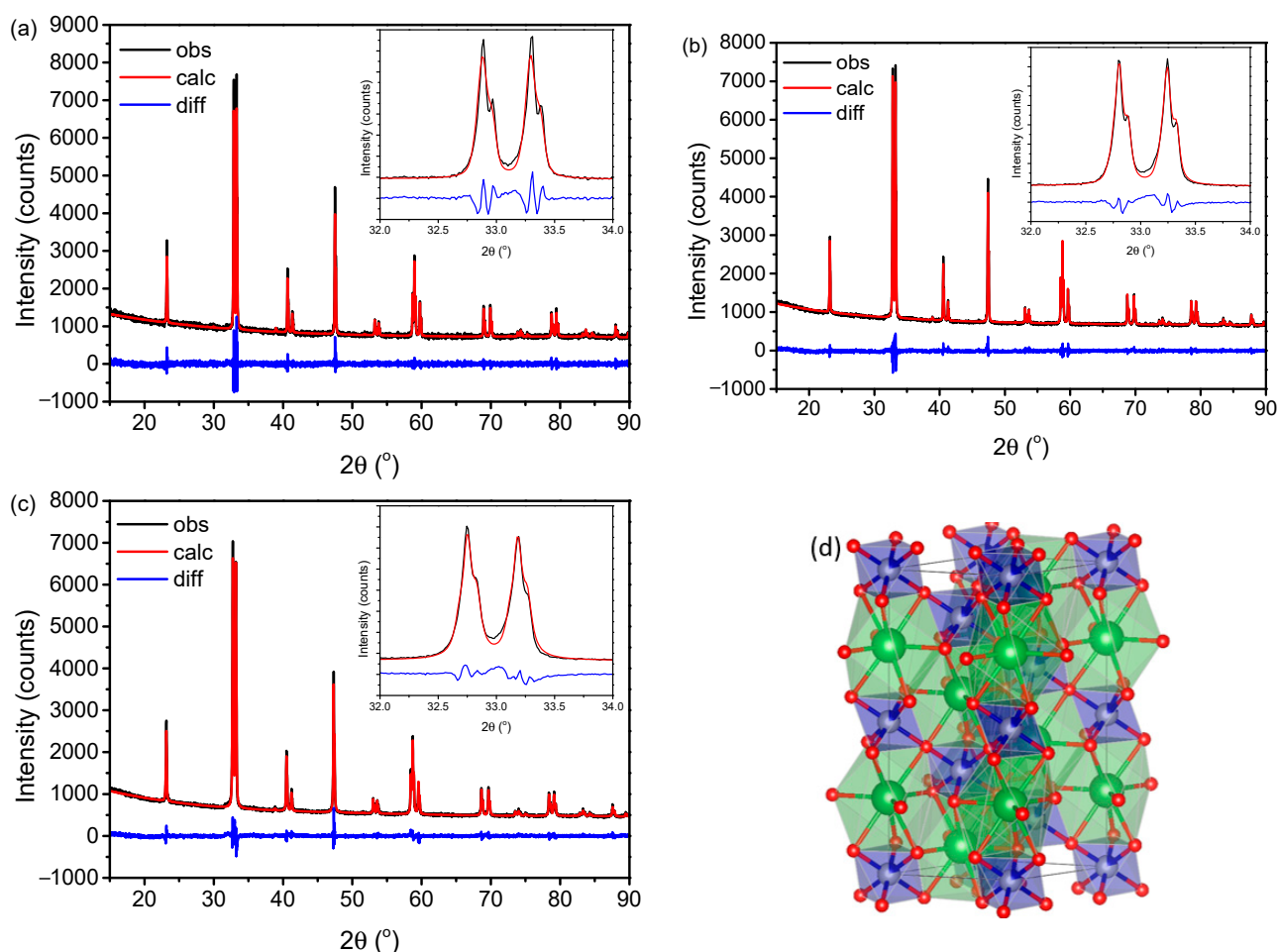


Figure 1. XRD pattern and graphical Rietveld refinement of perovskites, (a) $\text{LaCoO}_{3-\delta}$, (b) $\text{LaCo}_{0.8}\text{Ni}_{0.2}\text{O}_{3-\delta}$, and (c) $\text{LaCo}_{0.2}\text{Ni}_{0.8}\text{O}_{3-\delta}$. Insets show a zoom of the main perovskite peaks. (d) shows the atomic arrangement of the $\text{LaCo}_{0.2}\text{Ni}_{0.8}\text{O}_{3-\delta}$ structure using VESTA software [38], where the atoms are colored as follow: green = La, blue = Co, gray = Ni, and red = O.

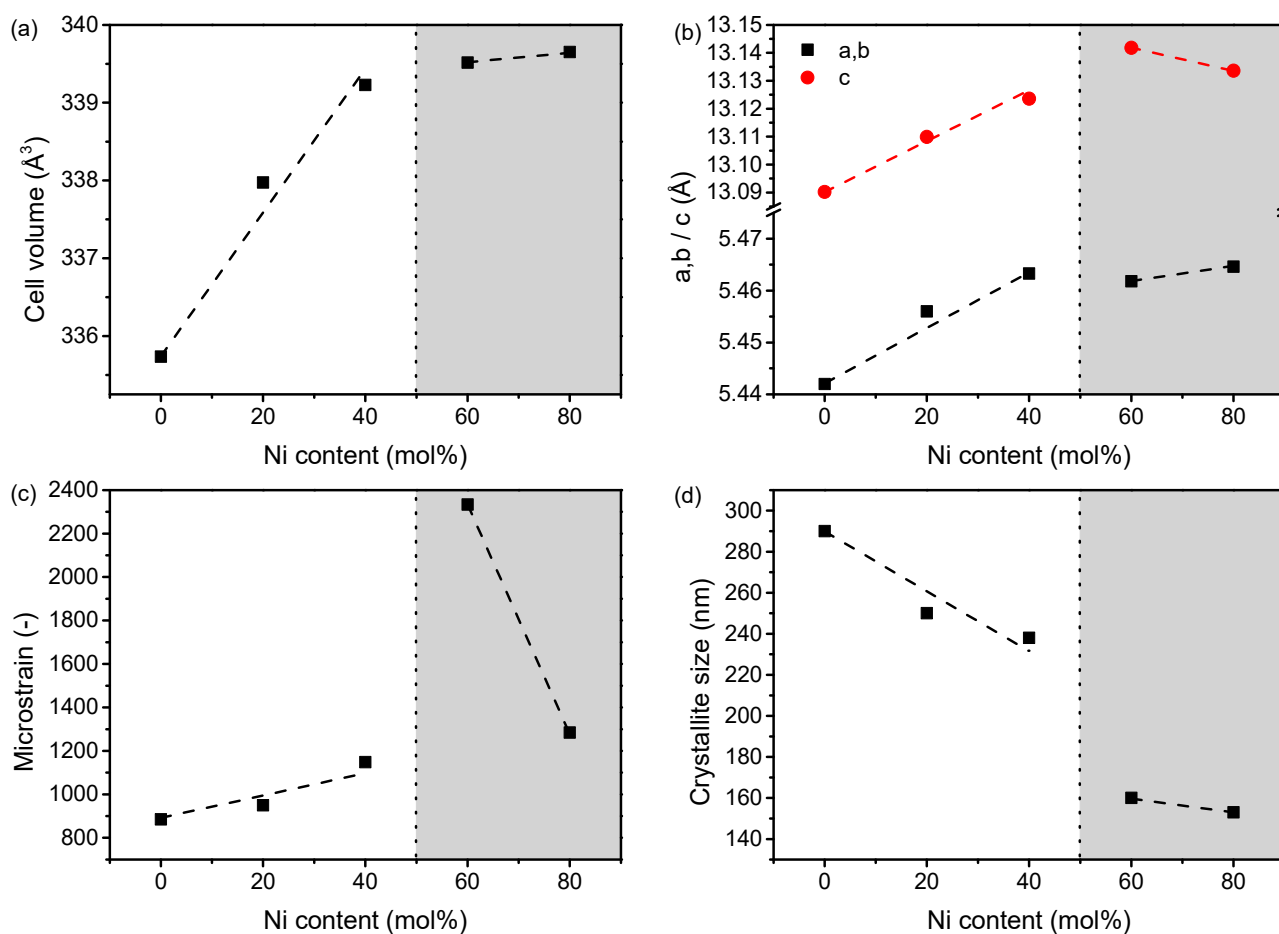


Figure 2. Structural information based on Rietveld refinement of the perovskite structures, (a) cell volume change, (b) a/b and c parameter changes, (c) microstrain, and (d) crystallite size. The dashed lines are guides for the eye, and the dotted line indicate the change from cobaltite (white area) to nickelate (grey area) structures.

The XPS analyses of $\text{LaCo}_{1-x}\text{Ni}_x\text{O}_{3-\delta}$ samples are summarized in Figure 3 and Table 1. Co 2p emission region shown in Figure 3a is typical of Co(III) as evidenced by the position at 779.3–779.8 eV of the Co 2p 3/2 component and the weak satellites with a shift, with respect to the main Co 2p peaks, of 9–10 eV [39,40]. The asymmetry of the peaks indicate the presence of a small component at 781.7 eV which is attributed to Co(II). A typical deconvolution is shown in Figure S2. In Table 1, the binding energy of the two Co 2p 3/2 components and the relative percentage of each component are indicated. The presence of nickel stabilizes the Co(III) form reaching a maximum of 90% of Co(III) in the structure for Ni = 0.6. The Co 2p region of $\text{LaCo}_{0.2}\text{Ni}_{0.8}\text{O}_{3-\delta}$ is not due to the low intensity of the cobalt peaks fitted, and the value reported is the position of the most intense peak.

Ni 2p emission overlaps with the region of La 3d 3/2 (see Figure 3c) and for this reason, nickel assessment has been done by means of Ni 3p emission. In this region, also Co 3p emissions are present and the direct comparison of the two peaks allows to estimate well the relative percentage of the two species. The region was fitted with two doublets (Ni 3p 3/2–Ni 3p 1/2 and Co 3p 3/2 and Co 3p 1/2) and a peak at higher binding energy due to Co satellite. An example of the fitting of this region is shown in Figure S3 and a comparison of all samples is shown in Figure 1b. The position of Ni 3p 3/2 at 67.1 eV is in accordance with the value found by Gao [41] for $\text{LaNi}_{0.8}\text{Co}_{0.2}\text{O}_{3-\delta}$. With the decreasing of the Ni content in the samples, the position of Co 3p 3/2 shifts to lower energy indicating a transfer of electrons from Co to Ni and thus an increase in Co oxidation state and a decrease in the Ni

oxidation state. This is in accordance with what has been discussed in literature about the increase of the oxidized cobalt with the increase of Nickel in the structure [41,42].

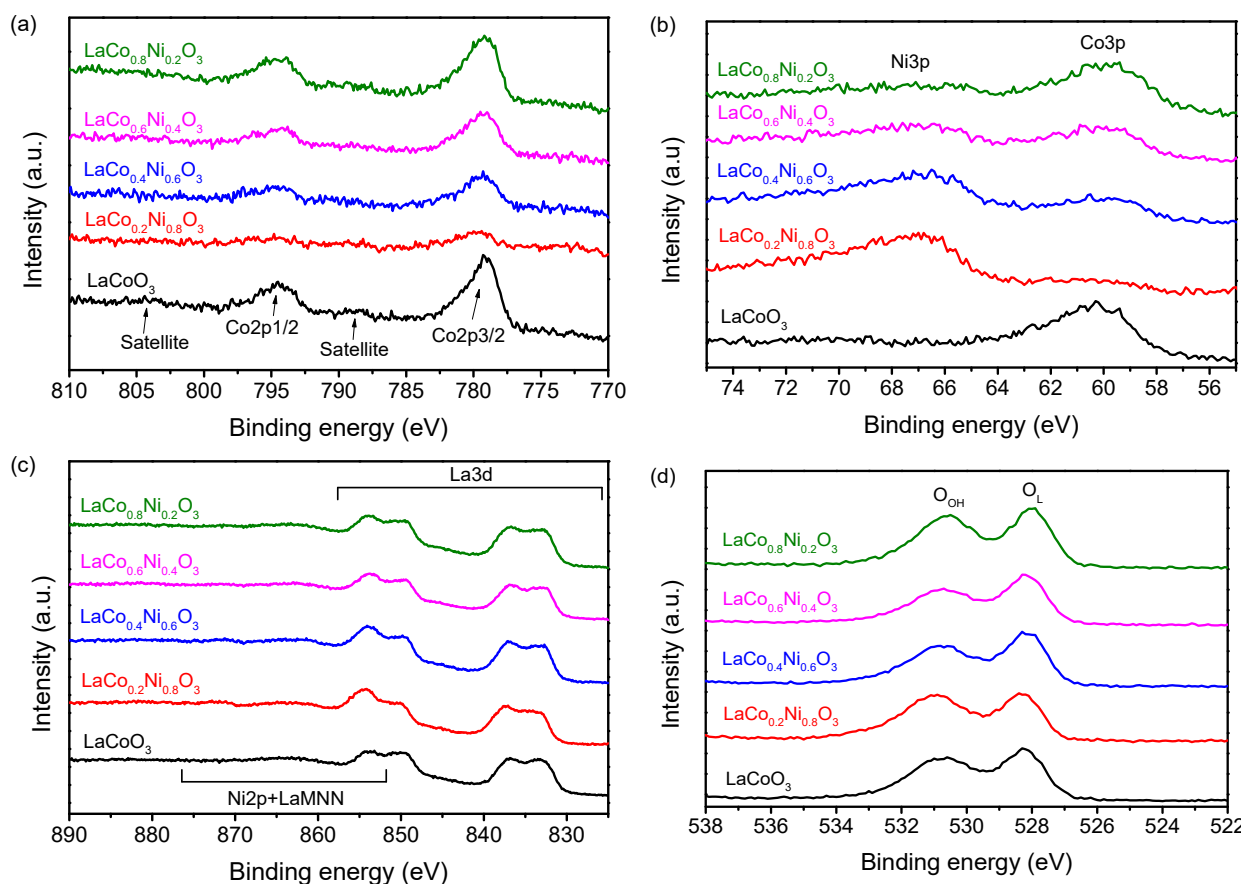


Figure 3. The XPS regions of: (a) Co 2p; (b) Ni 3p and Co 3p; (c) La 3d and Ni 2p; (d) O 1s of $\text{LaCo}_{1-x}\text{Ni}_x\text{O}_{3-\delta}$ samples.

Table 1. Co 2p 3/2, Ni 3p 3/2, O 1s binding energy (eV) (in parenthesis the relative percentage of each component is given) and surface Ni/Co, Co/La and Ni/La atomic ratio.

	Co 2p 3/2 (eV)	Ni 3p 3/2 (eV)	O 1s (eV)	Ni/Co ^a	Co/La ^a	Ni/La ^a
$\text{LaCo}_{0.2}\text{Ni}_{0.8}\text{O}_{3-\delta}$	779.8 ^b	67.1	528.3 (34%) 530.9 (66%)	10 (4.0)	0.1 (0.2)	0.9 (0.8)
$\text{LaCo}_{0.4}\text{Ni}_{0.6}\text{O}_{3-\delta}$	779.3 (90%) 781.7 (10%)	66.5	528.1 (40%) 530.7 (60%)	1.5 (1.5)	0.3 (0.4)	0.7 (0.6)
$\text{LaCo}_{0.6}\text{Ni}_{0.4}\text{O}_{3-\delta}$	779.2 (89%) 781.4 (11%)	66.5	528.2 (43%) 530.7 (57%)	1.25 (0.67)	0.5 (0.6)	0.6 (0.4)
$\text{LaCo}_{0.8}\text{Ni}_{0.2}\text{O}_{3-\delta}$	779.2 (89%) 781.4 (11%)	65.8	528.0 (40%) 530.6 (60%)	0.42 (0.25)	0.6 (0.8)	0.2 (0.2)
$\text{LaCoO}_{3-\delta}$	779.2 (78%) 780.9 (22%)	-	528.1 (38%) 530.7 (62%)	-	0.7 (1.0)	-

^a In parenthesis the nominal ratio are reported. ^b Spectrum not fitted.

O1s region (Figure 1d) shows the typical shape found in perovskite oxides. Two components are clearly distinguishable at 528.2 eV (due to oxygen from the lattice) and at 530.8 eV (due to surface OH^- species). No appreciable differences are found with the changes in composition.

The surface atomic ratio (compiled in Table 1) indicates an uneven distribution of metals. For all samples, the surface is enriched in nickel, while cobalt is concentrated more in the bulk of the material.

Additionally, FT-IR shows only three signals, around 420, 527, and 580 cm^{-1} corresponding to La-O stretching vibrations, Co-O stretching vibrations, and Co-O bending vibrations, respectively [43]. An example of a $\text{LaCoO}_{3-\delta}$ spectrum is found in Figure S4 in Supplementary Materials.

The band gap decreases with Ni-doping in the cobaltite-type composition, while it increases with Co-doping in the nickelate-type composition, showing an overall minimum among our samples at 40 mol% Ni-doping (Figure 4). The Kubelka–Munk plots are found in Figure S5. This trend and these values are similar to what is found in literature [44]. The non-linear change is possibly a result of a competition between the relaxation of the pure perovskites ($\text{LaCoO}_{3-\delta}$ and $\text{LaNiO}_{3-\delta}$) and their alloys ($\text{LaCo}_{1-x}\text{Ni}_x\text{O}_{3-\delta}$) as found for halide perovskites [45,46]. Thus, the non-linearity throughout the system might be caused by a change in structure from a cobalt-rich to nickel-rich composition. Within the given compositional ranges (cobaltite and nickelate), the band gap is linear, supporting the hypothesis that a change in main structure is the main reason for a lack of overall linearity. The change in band gap is small (<0.25 eV) compared to that found of Co-doped LaCrO_3 , where 30 mol% Co-doping results in an approximately 0.8 eV band decrease in band gap [47]. The small variation of band gap in these samples is like that of transition metal-doped (Cr and Co) BiFeO_3 perovskite, that shows a discontinuous change with doping, while a significant change occurs for Mn-doped BiFeO_3 [48]. It is worth noticing that measuring the band gap of Ni-doped LaCoO_3 perovskite powders using the diffuse reflectance spectroscopy method is difficult, due to the black color of the samples, resulting in a reflectance in the range 0–10%, which causes a significant effect in the determination of the band gap.

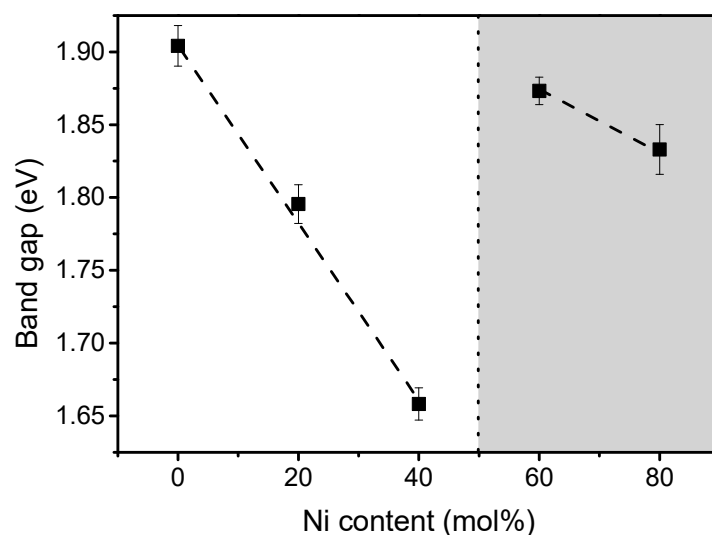


Figure 4. Band gap of synthesized $\text{LaCo}_{1-x}\text{Ni}_x\text{O}_{3-\delta}$ perovskites. Dashed lines are intended as guides for the eye, while the dotted line shows the transition from cobaltite (white area) to nickelate (gray area).

The morphology of the investigated samples is reasonably similar and all images showed agglomerated nanoparticles (Figure 5). The smallest particles are in the range of 200–300 nm for all compositions, similarly to what has previously been found for nickel-doped LaCoO_3 [49]. However, the average particle size seems to decrease with increasing nickel doping (Figure 5), in agreement with the change in crystallite size observed from the Rietveld refinement results (Table S1). The decrease in particle size of the powders by Ni-doping is also observed in the literature with aluminum doping [50]. The smaller

particles result in larger surface area (as seen in Figure 6), which is ideal for heterogeneous catalytic reactions.

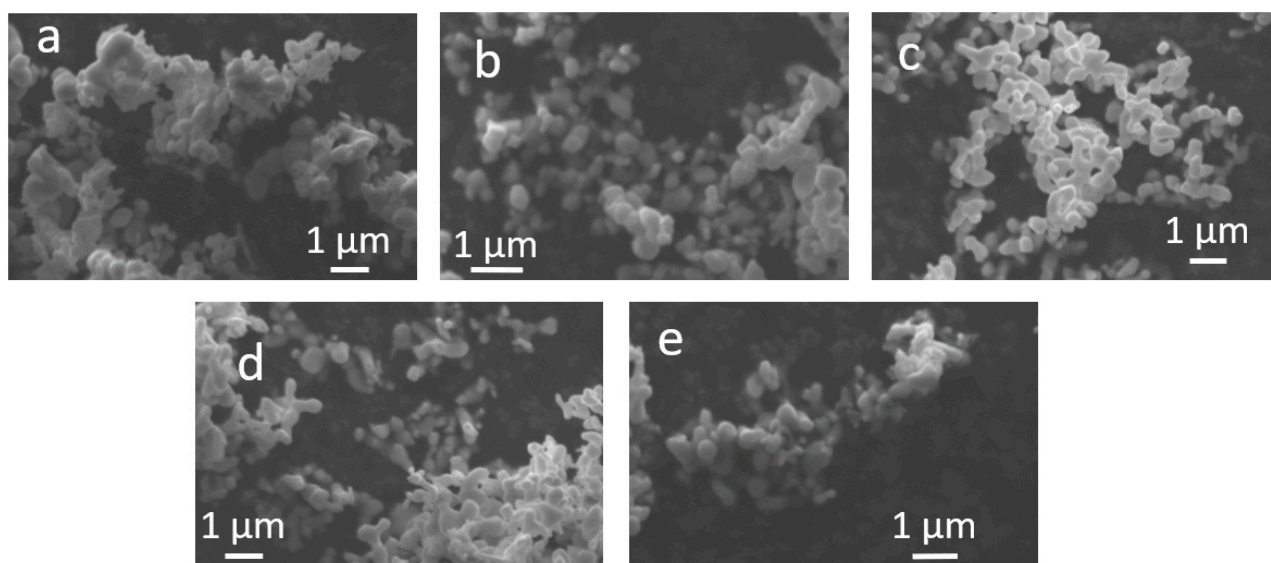


Figure 5. SEM images of the synthesized perovskites: (a) $\text{LaCoO}_{3-\delta}$, (b) $\text{LaCo}_{0.2}\text{Ni}_{0.8}\text{O}_{3-\delta}$, (c) $\text{LaCo}_{0.4}\text{Ni}_{0.6}\text{O}_{3-\delta}$, (d) $\text{LaCo}_{0.6}\text{Ni}_{0.4}\text{O}_{3-\delta}$, and (e) $\text{LaCo}_{0.8}\text{Ni}_{0.2}\text{O}_{3-\delta}$.

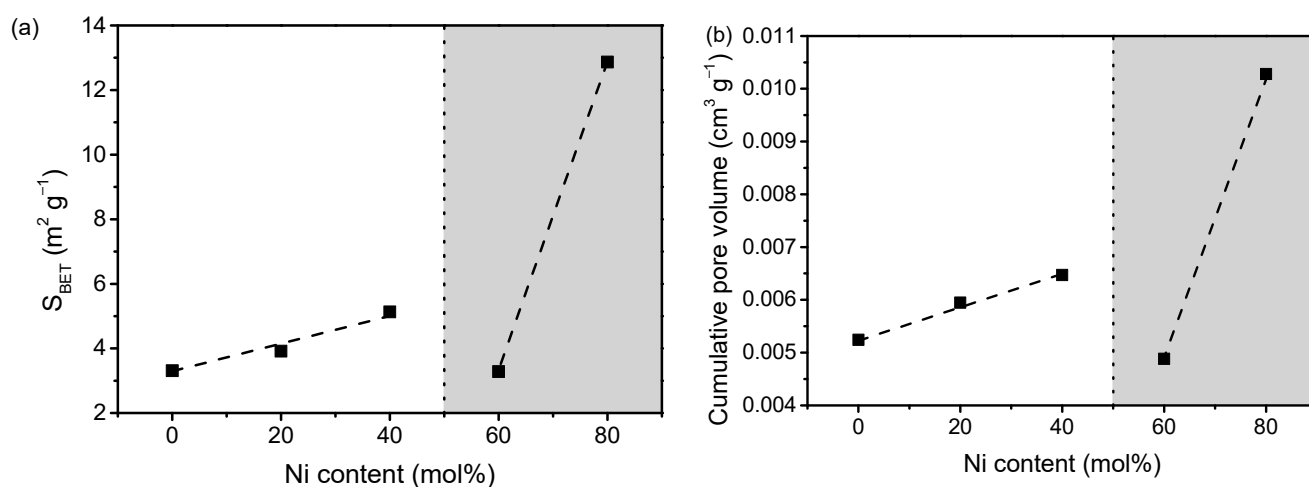


Figure 6. (a) BET surface area (S_{BET}) and (b) cumulative pore volume for $\text{LaCo}_{1-x}\text{Ni}_x\text{O}_{3-\delta}$ perovskites. Dashed lines are guides for the eye, and the dotted line illustrate the transition from cobaltite (white area) to nickelate (gray area).

The surface area increases with increasing Ni-content in the $\text{LaCo}_{1-x}\text{Ni}_x\text{O}_{3-\delta}$ perovskites (Figure 6), based on N_2 adsorption-desorption isotherms (Figure S6 in Supplementary Materials). At highest Ni-content, the surface area is approximately four times larger than for the pure $\text{LaCoO}_{3-\delta}$ perovskite. The reason for the significantly larger surface area at highest Ni-content and the smallest surface area at 60 mol% Ni is that the samples doped with 60–80 mol% Ni are no longer cobaltite-type, but instead Co-doped nickelates. Thus, a discontinuity is found in the trend of surface area, that increases with Ni-doping in the cobaltite area, while it decreases with Co-doping in the nickelate area, showing an overall minimum at 40 mol% Co-doping. This indicates that Ni is beneficial for obtaining a higher surface area compared to Co. The increase in surface area upon doping is expected from literature [49] where the surface area was doubled upon a 30 mol% Ni-doping of LaCoO_3 . The minimum surface area is found for 60 mol% Ni-doping. Similarly, lanthanide

perovskites have shown minima or maxima in surface area trends for 5–30 mol% doping in the $\text{LaNi}_{1-x}\text{Fe}_x\text{O}_3$ [51], $\text{LaCo}_{1-x}\text{Zn}_x\text{O}_3$ [52], and $\text{LaCo}_{1-x}\text{Cu}_x\text{O}_3$ systems [53].

The zeta potential values of the different perovskite suspensions in water are measured in the 2–10 pH range (Figure 7). In acidic environment, the perovskites exhibit a positively charged surface, with zeta potential ranging from 17–55 mV at pH of 2. The isoelectric point of the different suspensions is in the 4.35–6.10 pH range, with $\text{LaCoO}_{3-\delta}$ and $\text{LaCo}_{0.2}\text{Ni}_{0.8}\text{O}_{3-\delta}$ having a non-charged surface at lowest and highest pH, respectively. The isoelectric point seems to be higher for high content of nickel. In alkaline environment above the isoelectric point, the surface charge of the perovskites is negative. The zeta potential is important to have a stable suspension and to avoid agglomeration, as this would challenge the catalytic activity, due to a reduced available surface area for catalytic reactions. Furthermore, the surface charge of the perovskites in the suspension should be opposite to the charge of the pollutant, in this study rhodamine B, to increase the electrostatic attraction of the two compounds and thereby enhance the catalytic degradation [54]. As rhodamine B has a pKa of 4.2 [55], low pH degradation experiments are of interest to increase the attraction between the perovskites (positively charged at low pH) and rhodamine B (negatively charged at low pH) to enhance the catalytic reaction. Therefore, the degradation experiments presented in next section is carried out at pH of 2, as this is below both the pKa of rhodamine B and the point of zero charge of the investigated perovskites.

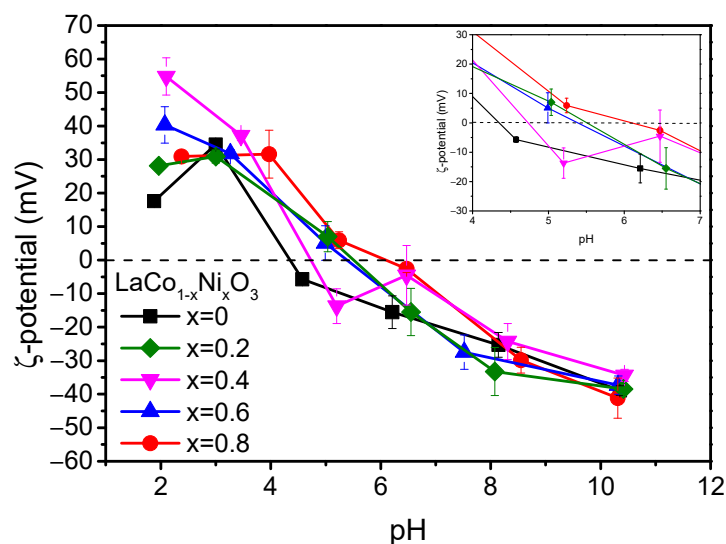


Figure 7. Effect of pH on Zeta potential of $\text{LaCo}_{1-x}\text{Ni}_x\text{O}_{3-\delta}$ perovskites.

2.2. Thermocatalytic Activity

Full UV–Vis spectra of rhodamine B (structure visualized in inset of Figure 8) during degradation at pH of 2 and 25 °C are displayed in Figure 8. Rhodamine B was degraded within 60 min using $\text{LaCoO}_{3-\delta}$ at room temperature. The degradation of rhodamine B is gradually visualized by the blueshift in maximum absorbance which is a result of deethylation of the structure [56,57]. The deethylation is clearly evidence that rhodamine B is degraded and not only adsorbed to the perovskite. Moreover, a degradation is found as the absorbance goes towards zero in the full range. The degradation mechanism plausibly follows the same pathway as discussed by Yu et al. [56], with an initial deethylation which is visible from Figure 8. This is followed by chromophore cleavage which might be a result of hydroxyl radical (OH) attack of the central carbon, causing a decolorization of the solution. In this study, we did not investigate the type of ROS, however, previously hydroxyl radicals and superoxide anions (O_2^-) have been suggested [24], which would agree well with the degradation of rhodamine B. The chromophore cleavage results in the formation of first organic acids due to oxidation followed by alcohols [56].

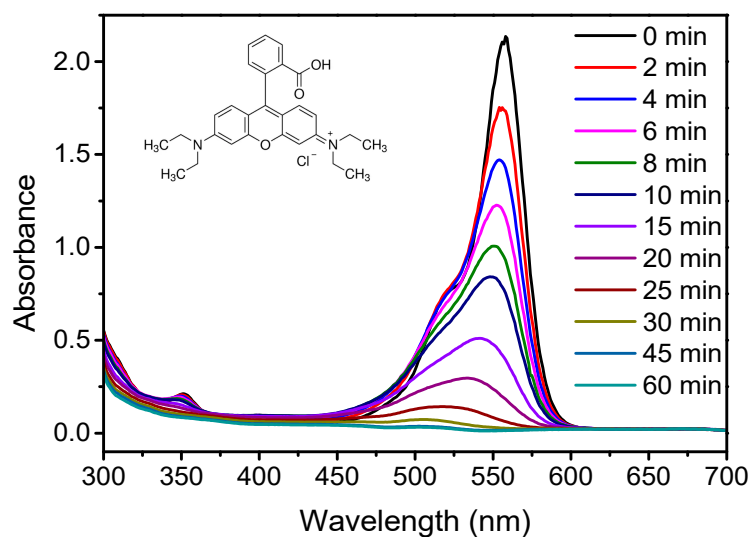


Figure 8. UV-Vis absorbance spectra of a rhodamine B solution during abatement with $\text{LaCoO}_{3-\delta}$ at 25 °C. The chemical structure of rhodamine B is shown as inset.

The degradation of rhodamine B with the different perovskites follows a pseudo-first order reaction as seen in Figure 9. As for the blueshift in Figure 8, the linear increase in $-\ln(c/c_0)$ proves a degradation of rhodamine B, as this would not have been the case for an adsorption process. The fastest degradation is found for the non-doped $\text{LaCoO}_{3-\delta}$ followed by highest Ni-doping and then decreasing with decreasing Ni-doping. All perovskite compositions degrade rhodamine B faster than LaCoO_3 is found to degrade tetracycline when used as photocatalyst [58]. The fastest degradation, found using $\text{LaCoO}_{3-\delta}$, agrees with previous findings that LaCoO_3 performs better than LaNiO_3 [8]. However, generally no specific trend in the optimum composition of Ni-doped $\text{LaCoO}_{3-\delta}$ perovskites in different catalytic processes has been found [43,59–61]. The better catalytic activity of $\text{LaCoO}_{3-\delta}$ might be a result of the Ni-enriched surface observed by XPS on the Ni-containing perovskites. The trend changes slightly from 300 mg L^{-1} to a lower concentration (100 mg L^{-1}) and higher concentration (500 mg L^{-1}) of perovskite, as can be found in Supplementary Materials Figure S7. For example, the activity of the undoped $\text{LaCoO}_{3-\delta}$ is smaller than for the $\text{LaCo}_{0.2}\text{Ni}_{0.8}\text{O}_{3-\delta}$ perovskite when using 100 mg L^{-1} of catalyst, whereas at higher catalyst concentration the $\text{LaCoO}_{3-\delta}$ is the best catalyst. This is possibly due to the fact that an increase in catalyst concentration compensates for the smaller surface area of $\text{LaCoO}_{3-\delta}$. On the other hand, the faster kinetics of the perovskite oxide catalyst with the highest Ni-doping degree is plausibly caused by its larger surface area compared to the other Ni-containing perovskites, as found in Figure 6. The difference in surface area is possibly also the reason why the 60 mol% doped perovskite is a worse catalyst than the 40 mol% doped one. Another reason could be the transition from cobaltite-type to nickelate-type perovskites, which changes the chemistry of the perovskite when exceeding 50 mol% Ni-doping, i.e., going from 40 mol% to 60 mol% Ni doping.

The concentration of perovskite used affects the kinetics of the rhodamine B degradation (Figure 10). By increasing the perovskite concentration from 100 mg L^{-1} to 500 mg L^{-1} , the kinetic constant increases by up to 600%, and the increase is more pronounced when increasing the concentration from 300 mg L^{-1} to 500 mg L^{-1} than from 100 mg L^{-1} to 300 mg L^{-1} . Interestingly, with increasing perovskite concentration, the difference among the perovskites becomes larger. At low concentration (100 mg L^{-1}), performance of $\text{LaCoO}_{3-\delta}$ and $\text{LaCo}_{0.2}\text{Ni}_{0.8}\text{O}_{3-\delta}$ are almost similar, but the $\text{LaCoO}_{3-\delta}$ perovskite is significantly more effective at 500 mg L^{-1} . This again might be a result of the compensation of low surface area by increasing the amount of perovskite of the undoped $\text{LaCoO}_{3-\delta}$. Another point worth commenting is that the reaction rate decreases with doping in both the cobaltite and nickelate composition range when comparing the kinetic constants in

Figure 10. This non-linear correlation between Ni-content and the reaction rate is possibly caused by the competition between the preferably larger surface area with increasing Ni-content, the difference in Co oxidation state, and the Ni-enrichment at the surface which limits the catalytic activity.

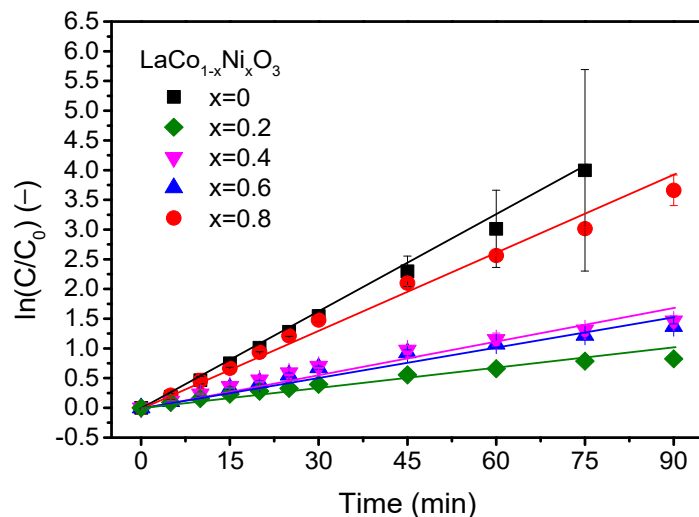


Figure 9. $\ln(c/c_0)$ vs. time of 300 mg L^{-1} perovskite for degradation of rhodamine B at $25 \text{ }^\circ\text{C}$. Lines represent best fits for first order kinetics.

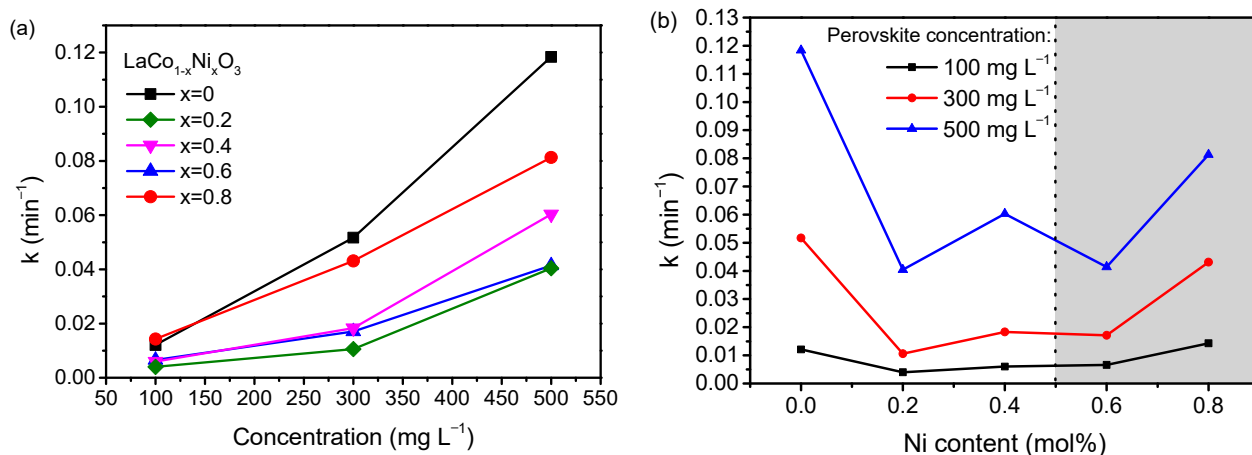


Figure 10. Change in kinetics with (a) perovskite concentration and (b) Ni content during degradation of rhodamine B at $25 \text{ }^\circ\text{C}$.

The stability of the perovskites as catalysts in the degradation of rhodamine B over consecutive cycles is investigated for $\text{LaCoO}_{3-\delta}$ and $\text{LaCo}_{0.2}\text{Ni}_{0.8}\text{O}_{3-\delta}$ (Figure S8). The activity decreases as function of cycles, suggesting deactivation or degradation of the catalyst itself. The second cycle for the $\text{LaCo}_{0.2}\text{Ni}_{0.8}\text{O}_{3-\delta}$ seems faster than the first cycle, but we expect that the decreasing activity as function of cycles is the most probable trend, given the significant decrease in activity at the third cycle. Previous studies showed leaching of elements from the perovskites, and this might be the reason for the continuous deactivation of our catalysts. For example, Hammouda et al. [10] showed leaching of both La and Co elements from $\text{LaCoO}_{3-\delta}$ perovskites, although the leaching stopped after 4–5 h. Manos et al. [62] found leaching of Co and Ni from LaCoO_3 and LaNiO_3 , respectively. Therefore, leaching is at least one explanation for the observed deactivation. Other authors found that leaching of elements can improve the catalytic stability by promoting a possible metal oxy(hydroxide) during self-construction that might be tuned based on thermodynamics [63,64]. On the other hand, we performed attenuated total reflectance (ATR)-FTIR to investigate possible

adsorption of the pollutant on the perovskites, and no change in the spectra, prior to and after catalytic used, is observed. The decreasing activity over time is a concern for an industrial use of perovskites, and extended research is required to understand the stability of perovskites in aqueous environments. Moreover, it needs to be investigated if the activity reduction is continuous or if the activity is stabilized after a certain time.

The rate of degradation of rhodamine B using the $\text{LaCoO}_{3-\delta}$ perovskite increases by increasing temperature in the dark, proving the thermal activation of the perovskites (Figure 11). This study is the first to prove the thermocatalytic behavior of the $\text{LaCo}_{1-x}\text{Ni}_x\text{O}_{3-\delta}$ system, although LaNiO_3 was previously found to act as thermocatalyst in the degradation of methyl orange [23]. The same trend is found for the Ni-doped $\text{LaCoO}_{3-\delta}$ and these are shown in Supplementary Materials (Figure S9). All the synthesized perovskites, except $\text{LaCo}_{0.4}\text{Ni}_{0.6}\text{O}_{3-\delta}$, degrade rhodamine B in <15 min at 60 °C and <45 min at 50 °C. Tummino et al. [65] showed approximately 40% degradation in 6 h under dark conditions and approximately 60% under solar irradiation in 6 h using $\text{Sr}_{0.85}\text{Ce}_{0.15}\text{FeO}_3$. Sun and Lin [66] synthesized $\text{SrTi}_{1-x}\text{Mn}_x\text{O}_3$ perovskites and degraded up to 50% of rhodamine B in dark and 80% under irradiation in 4 h. LaFeO_3 was shown to degrade rhodamine B up to 78% in 3 h under photocatalytic conditions by Wiranwetchayan et al. [67]. Comparing our results to catalytic degradation of rhodamine B in literature, the degradation of rhodamine B found for our $\text{LaCo}_{1-x}\text{Ni}_x\text{O}_{3-\delta}$ is much faster and can be considered competitive with the other literature findings.

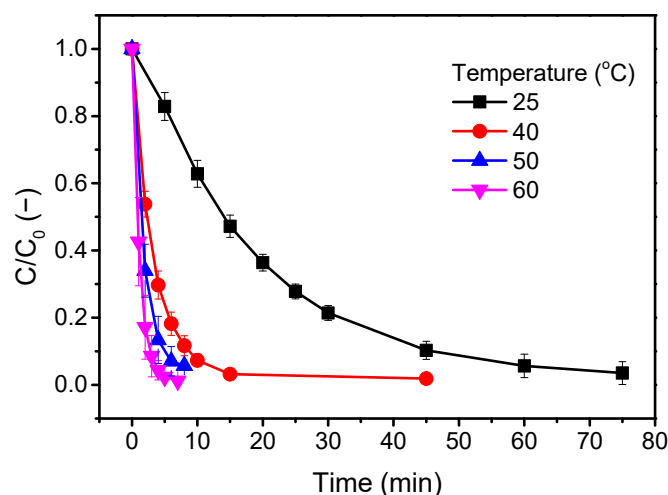


Figure 11. Temperature effect on thermocatalytic degradation of rhodamine B by $\text{LaCoO}_{3-\delta}$ with concentration of 300 mg L^{-1} .

In this study, we did not observe any correlation between the kinetic constant and the energy band gap. Indeed, band gap should affect the catalytic degradation, as the energy band gap determines the amount of energy required to excite electrons from the valence band to the conduction band and initiate the catalytic process. Nevertheless, the difference in energy band gap (Figure 4) among the different perovskites is relatively small.

The microstructural and textural features, such as crystal size and surface area, are important in catalytic processes, as small particles with large surface make more active sites available for the catalytic reaction. However, as can be seen in Figure 12, the highest catalytic activity is found for $\text{LaCoO}_{3-\delta}$ despite the fact that composition exhibits the smallest surface area, while the Ni-doped samples generally show an increase in reaction kinetics by increasing the surface area. The microstrain (Figure 2c) is here probably related more to the structural defects upon doping than to microstructural/morphological tensions, and its increase is often associated to a higher catalytic activity. According to that, the perovskite with 60 mol% Ni should show the highest catalytic activity, which is not the case. Therefore, the reason for the $\text{LaCoO}_{3-\delta}$ perovskite to be the best performing catalyst

in dark ambient degradation of rhodamine B must be related to the structural properties of the perovskite. Here, two options are possible, the Ni enrichment at the surface and the Co oxidation state. The Ni-enriched surface, found by XPS (Table 1), can be partly be caused by the segregated NiO. NiO has previously been found to lower the catalytic activity of mixed Co-Ni oxides [68]. However, considering the small amount of NiO observed in the XRD pattern, this seems unlikely to be the main reason for the worse catalytic activity of Ni-containing perovskites despite the fact that NiO might be the reason for the surface Ni enrichment. The second option is that the oxidation state of Co is the crucial parameter to control for these reactions. In fact, $\text{LaCoO}_{3-\delta}$ has a considerably higher amount of Co(II) in the structure whereas the Co(III) is stabilized upon Ni doping, with a high amount (~90%) of Co(III), as seen from the XPS results (Table 1). This is in agreement with other literature results concerning another oxidation reaction, the catalytic oxidation of CO, where Co(II) was found preferred over Co(III) [69,70]. Therefore, in the case of dark ambient degradation of rhodamine B using Ni-doped $\text{LaCoO}_{3-\delta}$ perovskites, the most crucial parameter to control is the Co(II)/Co(III) ratio.

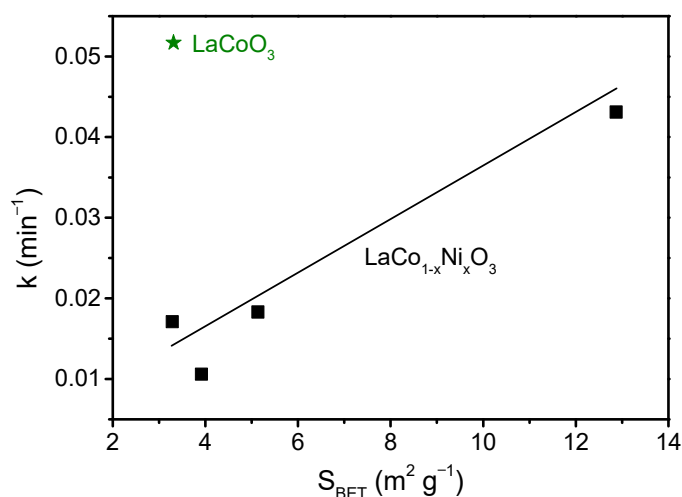


Figure 12. Correlations of kinetic constant and surface area determined by BET isotherm. The black squares are data for the Ni-doped samples and the green star is the symbol of the undoped LaCoO_3 . The black line is a guide for the eye for the Ni-doped series.

3. Materials and Methods

3.1. Perovskite Oxide Powders Synthesis

$\text{LaCo}_{1-x}\text{Ni}_x\text{O}_{3-\delta}$ ($x = 0, 0.2, 0.4, 0.6,$ and 0.8) were synthesized by solution combustion synthesis. Stoichiometric amounts of $\text{La}(\text{NO}_3)_3 \cdot 6\text{H}_2\text{O}$ (Th. Geyer, Renningen, Germany, purity 98%), $\text{Co}(\text{NO}_3)_2 \cdot 6\text{H}_2\text{O}$ (Th. Geyer, Renningen, Germany, purity 98%), and $\text{Ni}(\text{NO}_3)_2 \cdot 6\text{H}_2\text{O}$ (Alfa Aesar, Kandel, Germany, purity 98%) were dissolved in 190 mL deionized water. The amount of weighed chemicals are found in Table S3 in Supplementary Materials. Citric acid (Carl Roth, Karlsruhe, Germany, purity $\geq 99.5\%$) was added as organic fuel with a citric acid-to-metal cations molar ratio of 2. NH_4NO_3 (Sigma Aldrich, Steinheim, Germany, purity $\geq 99.5\%$) was added as an additional oxidant to achieve a reducers-to-oxidizers ratio of 1.5, and pH was adjusted to 6 by adding NH_4OH solution (25 wt%). The solution was left on a hot plate controlled at 80°C using a connected Vertex thermometer for evaporation of the water under magnetic stirring until a gel was formed. When the gel was formed, the magnetic bar was removed, and the hot plate was set to 310°C under the fume hood to cause the self-ignition. The as-burned powder was crushed and calcined at 1000°C for 5 h with a 2°C min^{-1} temperature ramp.

3.2. Perovskite Oxide Powders Characterization

The bulk structural properties of the synthesized perovskites was investigated by XRD on a PANalytical Empyrean diffractometer (Almelo, The Netherlands), with Cu K α radiation ($\lambda = 1.5418 \text{ \AA}$), a voltage of 45 kV, and a current of 40 mA. The obtained diffraction patterns were analyzed quantitatively by Rietveld refinement using the GSAS-II software [71]. A Chebyshev polynomial with seven coefficients was chosen for the background. Sample displacement was refined together with the unit cell of the crystal phase. The size of the particles was fitted isotropic and the microstrain of the structure was fitted with the atomic coordinates and the atomic displacement parameter (U_{iso}) for the most abundant B-site atom. From fitting results, the structural information, in particular the cell edge lengths and relative phase composition, was obtained. The agreement factors, describing the goodness of the Rietveld fitting, were acceptable. The cif files for the starting model were taken from the ICDD PDF4+ database: LaCoO₃ (01-080-3118), LaCo_{0.2}Ni_{0.8}O₃ (00-066-0346), LaCo_{0.4}Ni_{0.6}O₃ (00-005-0602), LaCo_{0.6}Ni_{0.4}O₃, (01-073-2813), and LaCo_{0.8}Ni_{0.2}O₃ (01-073-2813).

The XPS spectra were acquired by an ESCALAB MkII (VG Scientific—East Grinstead, UK) spectrometer equipped with a standard Al excitation source and 5-channeltron as detection system. The measurements were performed operating at 50 eV constant pass energy and the binding energy (BE) scale was calibrated positioning the C 1s peak from adventitious carbon at BE = 285.0 eV. The obtained spectra were processed by CasaXPS software.

Band gap was obtained through a Kubelka–Munk plot of the UV–Vis data from the perovskites. The diffuse reflectance spectra were gathered in the range 200–800 nm by a UV–Visible Spectrophotometer, PerkinElmer Lambda 1050 (Waltham, MA, USA), with an integrating sphere using BaSO₄ as a reference material.

The morphology of the synthesized perovskites was analyzed by scanning electron microscopy (SEM) using a Zeiss EVO 60 microscope (Oberkochen, Germany). The perovskite powder was gently placed on carbon tape prior to entering the SEM, and no further coating was applied.

Specific surface area (Brunauer, Emmet, and Teller's method [72]) and pore size distributions (Barrett, Joyner, and Halenda's method [73]) were evaluated by nitrogen adsorption/desorption measurements at $-196 \text{ }^\circ\text{C}$, using ASAP 2020 Plus (Micromeritics, Norcross, GA, USA). All the samples were pre-treated under vacuum at $250 \text{ }^\circ\text{C}$ ($10 \text{ }^\circ\text{C min}^{-1}$) for 1 h prior to the measurements.

Zeta potential was measured on a Zetasizer Nano ZS (Malvern, UK). The samples were dispersed in a 5 mM NaCl solution to ensure a higher conductivity and pH adjusted with HCl or NaOH to the desired pH. After the initial pH adjustment, the samples were sonicated for 10 min at 35 kHz and placed on a magnetic stirrer for further pH adjustment if needed. After each adjustment, the suspension was left to equilibrate for 5 min.

3.3. Thermocatalytic Tests

A measure of 10 mg L^{-1} of rhodamine B was prepared, and pH value was adjusted to 2. Then, 100 mL of solution was poured into a cap bottle and placed in a Bandelin RK 100 H sonication bath at a frequency of 35 kHz with temperature control. The sonication was used to keep the perovskite particles in suspension as it was found that the particles either agglomerated or precipitated on the glass surface without the sonication. The temperature of the rhodamine B solution was varied between $25 \text{ }^\circ\text{C}$ and $60 \text{ }^\circ\text{C}$ to test the thermocatalytic properties of the powders. When the desired temperature was reached, the perovskite powder was added, and the solution was stirred for 15 s using a magnetic stirrer before inserting it again into the sonication bath. The reaction start was when the perovskite powder was added to the rhodamine B solution. The temperature in the cap bottle was monitored with a thermometer and kept constant within $1\text{--}2 \text{ }^\circ\text{C}$ of the desired temperature. The catalytic reaction was stopped when the measured absorbance of the dye was $\leq 5\%$ of the initial absorbance or, alternatively, after 90 min of run-time. We note that the absorbance did not change for the rhodamine B solution when perovskites were not added. Samples

were collected and filtered through a 0.45 μm RC filter for absorbance measurements and then measured on a Spectronic 20 Genesys at 558 nm. A cover was placed over the samples between measurements to minimize external light interference.

4. Conclusions

Ni-doped $\text{LaCoO}_{3-\delta}$ perovskites were synthesized by solution combustion synthesis and used as thermocatalysts for the degradation of rhodamine B in the 25–60 °C temperature range under dark. Thermocatalytic results have shown that the undoped $\text{LaCoO}_{3-\delta}$ exhibits the greatest activity ($k = 0.052 \text{ min}^{-1}$ at 300 mg L^{-1} perovskite) in the degradation of rhodamine B, with degradation within 60 min at room temperature and <10 min at 60 °C. The introduction of Ni in the formulation caused a decrease in perovskite oxide catalytic activity ($k = 0.017 \text{ min}^{-1}$ at 300 mg L^{-1} of $\text{LaNi}_{0.6}\text{Co}_{0.4}\text{O}_{3-\delta}$) and this might be ascribed to the increase and stabilization of the Co(III) in the perovskite structure of the Ni-doped samples, where Co(III) content increased from 78% to 89–90%. However, at lower catalyst concentration (100 mg L^{-1}), the kinetics of the 80 mol% Ni-doped- $\text{LaCoO}_{3-\delta}$ was found better than the undoped perovskite, due to the higher surface area of the Ni-doped perovskite powder. For the Ni-doped $\text{LaCoO}_{3-\delta}$ perovskites, the catalytic activity increased with increasing Ni-content, in agreement with the increase in surface area (from 3.31 to 12.87 $\text{m}^2 \text{ g}^{-1}$), and thus, the catalytic activity was determined by a balance between the surface oxidation state of Co and surface area.

Supplementary Materials: The following supporting information can be downloaded at: <https://www.mdpi.com/article/10.3390/catal13020325/s1>, Table S1. Crystal space group, lattice parameters, crystal size, density, and fitting parameters from Rietveld refinement for all synthesized perovskites; Table S2. Atomic positions and thermal parameters of $\text{LaCoO}_{3-\delta}$ and $\text{LaCo}_{0.2}\text{Ni}_{0.8}\text{O}_{3-\delta}$ from Rietveld refinements. Differences compared to that in the ICDD database is shown in brackets; Table S3. Amounts of chemicals used for synthesizing of each perovskite composition; Figure S1. X-ray diffractogram of synthesized LaNiO_3 containing impurities; Figure S2. Fitted Co 2p region of $\text{LaCoO}_{3-\delta}$. Bold line Co 2p 3/2, dashed line Co 2p 1/2; green dotted line Co satellites; Figure S3. Fitted Co 2p, Ni 2p XPS region of $\text{LaCo}_{0.6}\text{Ni}_{0.4}\text{O}_{3-\delta}$; Figure S4. ATR-FTIR of $\text{LaCoO}_{3-\delta}$. Inset shows a zoom of the main signals; Figure S5. Kubelka–Munk plots for determination of the energy band gap; Figure S6. N_2 adsorption and desorption isotherms for the synthesized perovskites (a) $\text{LaCoO}_{3-\delta}$, (b) $\text{LaCo}_{0.8}\text{Ni}_{0.2}\text{O}_{3-\delta}$, (c) $\text{LaCo}_{0.6}\text{Ni}_{0.4}\text{O}_{3-\delta}$, (d) $\text{LaCo}_{0.4}\text{Ni}_{0.6}\text{O}_{3-\delta}$, and (e) $\text{LaCo}_{0.2}\text{Ni}_{0.8}\text{O}_{3-\delta}$; Figure S7. Degradation of rhodamine B at perovskite concentrations of (a) 100 mg L^{-1} and (b) 500 mg L^{-1} ; Figure S8. Stability of (a) $\text{LaCoO}_{3-\delta}$ and (b) $\text{LaCo}_{0.2}\text{Ni}_{0.8}\text{O}_{3-\delta}$ during 3 cycles of catalytic degradation of rhodamine B at 25 °C; Figure S9. Temperature effect on catalytic activity for (a) $\text{LaCo}_{0.8}\text{Ni}_{0.2}\text{O}_{3-\delta}$, (b) $\text{LaCo}_{0.6}\text{Ni}_{0.4}\text{O}_{3-\delta}$, (c) $\text{LaCo}_{0.4}\text{Ni}_{0.6}\text{O}_{3-\delta}$, and (d) $\text{LaCo}_{0.2}\text{Ni}_{0.8}\text{O}_{3-\delta}$.

Author Contributions: Conceptualization, B.H.C. and M.B.Ø.; methodology, B.H.C. and M.B.Ø.; validation, B.H.C.; formal analysis, B.H.C., F.D. and V.L.P.; investigation, B.H.C., F.D. and V.L.P.; resources, M.K.J.; writing—original draft preparation, M.B.Ø.; writing—review and editing, B.H.C., F.D., V.L.P., M.K.J. and V.B.; visualization, M.B.Ø., F.D. and V.L.P.; supervision, V.B. and M.B.Ø.; project administration, M.B.Ø.; funding acquisition, F.D. and M.K.J. All authors have read and agreed to the published version of the manuscript.

Funding: This work was supported by the Villum Foundation (grant no. 00028236).

Data Availability Statement: The data are contained within the article or Supplementary Materials.

Acknowledgments: CNR-ISMN Palermo Technician Gabriele Gallì is greatly acknowledged for his support in the N_2 adsorption measurements. We thank Peter K. Kristensen (Aalborg University) for his assistance with SEM and DRS analyses.

Conflicts of Interest: The authors declare no conflict of interest.

References

1. Tilley, R.J.D. *Perovskites: Structure-Property Relationships*, 1st ed.; John Wiley & Sons Ltd.: Chichester, UK, 2016.
2. Tanaka, H.; Misono, M. Advances in Designing Perovskite Catalysts. *Curr. Opin. Solid State Mater. Sci.* **2001**, *5*, 381–387. [[CrossRef](#)]

3. Nitadori, T.; Ichiki, T.; Misono, M. Catalytic Properties of Perovskite-Type Mixed Oxides (ABO₃) Consisting of Rare Earth and 3d Transition Metals. The Roles of the A- and B-Site Ions. *Bull. Chem. Soc. Jpn.* **1988**, *61*, 621–626. [[CrossRef](#)]
4. Gao, P.; Yan, S.; Tian, X.; Nie, Y.; Wang, Y.; Deng, Y.; Tu, J. Identification and Manipulation of Active Centers on Perovskites to Enhance Catalysis of Peroxymonosulfate for Degradation of Emerging Pollutants in Water. *J. Hazard Mater.* **2022**, *424*, 127384. [[CrossRef](#)]
5. Lin, N.; Gong, Y.; Wang, R.; Wang, Y.; Zhang, X. Critical Review of Perovskite-Based Materials in Advanced Oxidation System for Wastewater Treatment: Design, Applications and Mechanisms. *J. Hazard Mater.* **2022**, *424*, 127637. [[CrossRef](#)]
6. Suntivich, J.; Gasteiger, H.A.; Yabuuchi, N.; Nakanishi, H.; Goodenough, J.B.; Shao-Horn, Y. Design Principles for Oxygen-Reduction Activity on Perovskite Oxide Catalysts for Fuel Cells and Metal-Air Batteries. *Nat. Chem.* **2011**, *3*, 546–550. [[CrossRef](#)]
7. Suntivich, J.; May, K.J.; Gasteiger, H.A.; Goodenough, J.B.; Shao-horn, Y. A Perovskite Oxide Optimized for Molecular Orbital Principles. *Science* **2011**, *334*, 2010–2012. [[CrossRef](#)]
8. Lin, K.Y.A.; Chen, Y.C.; Lin, Y.F. LaMO₃ Perovskites (M=Co, Cu, Fe and Ni) as Heterogeneous Catalysts for Activating Peroxymonosulfate in Water. *Chem. Eng. Sci.* **2017**, *160*, 96–105. [[CrossRef](#)]
9. Haron, W.; Wisitsoraat, A.; Sirimahachai, U.; Wongnawa, S. A Simple Synthesis and Characterization of LaMO₃ (M=Al, Co, Fe, Gd) Perovskites via Chemical Co-Precipitation Method. *Songklanakarim J. Sci. Technol.* **2018**, *40*, 484–491. [[CrossRef](#)]
10. Hammouda, S.B.; Zhao, F.; Safaei, Z.; Srivastava, V.; Lakshmi Ramasamy, D.; Iftekhar, S.; Kalliola, S.; Sillanpää, M. Degradation and Mineralization of Phenol in Aqueous Medium by Heterogeneous Monopersulfate Activation on Nanostructured Cobalt Based-Perovskite Catalysts ACoO₃ (A=La, Ba, Sr and Ce): Characterization, Kinetics and Mechanism Study. *Appl. Catal. B* **2017**, *215*, 60–73. [[CrossRef](#)]
11. Gao, P.; Tian, X.; Nie, Y.; Yang, C.; Zhou, Z.; Wang, Y. Promoted Peroxymonosulfate Activation into Singlet Oxygen over Perovskite for Ofloxacin Degradation by Controlling the Oxygen Defect Concentration. *Chem. Eng. J.* **2019**, *359*, 828–839. [[CrossRef](#)]
12. Peña, M.A.; Fierro, J.L.G. Chemical Structures and Performance of Perovskite Oxides. *Chem. Rev.* **2001**, *101*, 1981–2017. [[CrossRef](#)]
13. Ghafoor, A.; Bibi, I.; Majid, F.; Ata, S.; Nouren, S.; Raza, Q.; Iqbal, M. Yttrium and Cobalt Doped LaNiO₃ Nanoparticles Synthesis and Solar Light Driven Photocatalytic Removal of Rhodamine, B. *Mater. Res. Bull.* **2023**, *159*, 112112. [[CrossRef](#)]
14. Lan, C.; Zhao, S.; Xu, T.; Ma, J.; Hayase, S.; Ma, T. Investigation on Structures, Band Gaps, and Electronic Structures of Lead Free La₂NiMnO₆ Double Perovskite Materials for Potential Application of Solar Cell. *J. Alloys Compd.* **2016**, *655*, 208–214. [[CrossRef](#)]
15. Grinberg, I.; West, D.V.; Torres, M.; Gou, G.; Stein, D.M.; Wu, L.; Chen, G.; Gallo, E.M.; Akbashev, A.R.; Davies, P.K.; et al. Perovskite Oxides for Visible-Light-Absorbing Ferroelectric and Photovoltaic Materials. *Nature* **2013**, *503*, 509–512. [[CrossRef](#)]
16. Lee, S.; Levi, R.D.; Qu, W.; Lee, S.C.; Randall, C.A. Band-Gap Nonlinearity in Perovskite Structured Solid Solutions. *J. Appl. Phys.* **2010**, *107*, 23523. [[CrossRef](#)]
17. Lu, Y.; Ma, A.; Yu, Y.; Tan, R.; Liu, C.; Zhang, P.; Liu, D.; Gui, J. Engineering Oxygen Vacancies into LaCoO₃ Perovskite for Efficient Electrocatalytic Oxygen Evolution. *ACS Sustain. Chem. Eng.* **2019**, *7*, 2906–2910. [[CrossRef](#)]
18. Chen, H.; Motuzas, J.; Martens, W.; Diniz da Costa, J.C. Surface and Catalytic Properties of Stable Me(Ba, Ca and Mg)SrCoO for the Degradation of Orange II Dye under Dark Conditions. *Appl. Surf. Sci.* **2018**, *450*, 292–300. [[CrossRef](#)]
19. Chen, H.; Motuzas, J.; Martens, W.; Diniz da Costa, J.C. Ceramic Metal Oxides with Ni²⁺ Active Phase for the Fast Degradation of Orange II Dye under Dark Ambient. *Ceram. Int.* **2018**, *44*, 6634–6640. [[CrossRef](#)]
20. Chen, H.; Motuzas, J.; Martens, W.; Diniz da Costa, J.C. Improved Dark Ambient Degradation of Organic Pollutants by Cerium Strontium Cobalt Perovskite. *J. Environ. Sci.* **2020**, *90*, 110–118. [[CrossRef](#)]
21. Østergaard, M.B.; Strunck, A.B.; Boffa, V.; Jørgensen, M.K. Kinetics of Strontium Carbonate Formation on a Ce-Doped SrFeO₃ Perovskite. *Catalysts* **2022**, *12*, 265. [[CrossRef](#)]
22. Luo, X.; Su, C.; Chen, Z.; Xu, L.; Zhao, L.; Zhao, J.; Qiu, R.; Huang, Z. Mechanochemical Synthesis of La-Sr-Co Perovskite Composites for Catalytic Degradation of Doxycycline in the Dark: Role of Oxygen Vacancies. *Sep. Purif. Technol.* **2022**, *300*, 121891. [[CrossRef](#)]
23. Zhong, W.; Jiang, T.; Dang, Y.; He, J.; Chen, S.Y.; Kuo, C.H.; Kriz, D.; Meng, Y.; Meguerdichian, A.G.; Suib, S.L. Mechanism Studies on Methyl Orange Dye Degradation by Perovskite-Type LaNiO_{3-δ} under Dark Ambient Conditions. *Appl. Catal. A Gen.* **2018**, *549*, 302–309. [[CrossRef](#)]
24. Chen, H.; Ku, J.; Wang, L. Thermal Catalysis under Dark Ambient Conditions in Environmental Remediation: Fundamental Principles, Development, and Challenges. *Chin. J. Catal.* **2019**, *40*, 1117–1134. [[CrossRef](#)]
25. Al-Buriah, A.K.; Al-Gheethi, A.A.; Senthil Kumar, P.; Radin Mohamed, R.M.S.; Yusof, H.; Alsharif, A.F.; Khalifa, N.A. Elimination of Rhodamine B from Textile Wastewater Using Nanoparticle Photocatalysts: A Review for Sustainable Approaches. *Chemosphere* **2022**, *287*, 132162. [[CrossRef](#)]
26. Yusuf, T.L.; Orimolade, B.O.; Masekela, D.; Mamba, B.; Mabuba, N. The Application of Photoelectrocatalysis in the Degradation of Rhodamine B in Aqueous Solutions: A Review. *RSC Adv.* **2022**, *12*, 26176–26191. [[CrossRef](#)]
27. Gou, Y.; Liang, X.; Chen, B. Porous Ni-Co Bimetal Oxides Nanosheets and Catalytic Properties for CO Oxidation. *J. Alloys Compd.* **2013**, *574*, 181–187. [[CrossRef](#)]
28. Wu, Z.; Niu, H.; Chen, J.; Chen, J. Metal-organic frameworks-derived hierarchical Co₃O₄/CoNi-layered double oxides nanocages with the enhanced catalytic activity for toluene oxidation. *Chemosphere* **2021**, *280*, 130801. [[CrossRef](#)]
29. Deganello, F.; Tyagi, A.K. Solution Combustion Synthesis, Energy and Environment: Best Parameters for Better Materials. *Prog. Cryst. Growth Charact. Mater.* **2018**, *64*, 23–61. [[CrossRef](#)]

30. Colomer, M.T.; Fumo, D.A.; Jurado, J.R.; Segadães, A.M. Non-Stoichiometric $\text{La}_{(1-x)}\text{NiO}_{(3-\delta)}$ Perovskites Produced by Combustion Synthesis. *J. Mater. Chem.* **1999**, *9*, 2505–2510. [[CrossRef](#)]
31. Alonso, J.A.; Martínez-Lope, M.J.; Falcón, H.; Carbonio, R.E. On the Correlation of Ni Oxidation States and Electronic Conductivity of $(\text{R,A})\text{NiO}_{3-\delta}$ (R=lanthanides, A=alkaline Earths, Th) Perovskites with Catalytic Activity for H_2O_2 Decomposition. *Phys. Chem. Chem. Phys.* **1999**, *1*, 3025–3030. [[CrossRef](#)]
32. Sánchez, R.D.; Causa, M.T.; Seoane, A.; Rivas, J.; Rivadulla, F.; López-Quintela, M.A.; Pérez Cacho, J.J.; Blasco, J.; García, J. Metal–Insulator Transition and Magnetic Properties of $\text{La}_{1-x}\text{Eu}_x\text{NiO}_3$ ($0 \leq x \leq 1$). *J. Solid State Chem.* **2000**, *151*, 1–11. [[CrossRef](#)]
33. Haas, O.; Struis, R.P.W.J.; McBreen, J.M. Synchrotron X-Ray Absorption of LaCoO_3 Perovskite. *J. Solid State Chem.* **2004**, *177*, 1000–1010. [[CrossRef](#)]
34. Vyshatko, N.P.; Kharton, V.V.; Shaula, A.L.; Marques, F.M.B. Powder X-ray diffraction study of $\text{LaCo}_{0.5}\text{Ni}_{0.5}\text{O}_{3-\delta}$ and $\text{LaCo}_{0.5}\text{Fe}_{0.5}\text{O}_{3-\delta}$. *Powder Diffr.* **2003**, *18*, 159–161. [[CrossRef](#)]
35. Simböck, J.; Ghiasi, M.; Schönebaum, S.; Simon, U.; de Groot, F.M.F.; Palkovits, R. Electronic Parameters in Cobalt-Based Perovskite-Type Oxides as Descriptors for Chemocatalytic Reactions. *Nat. Commun.* **2020**, *11*, 652. [[CrossRef](#)] [[PubMed](#)]
36. Shannon, R.D. Revised Effective Ionic Radii and Systematic Studies of Interatomic Distances in Halides and Chalcogenides. *Acta Cryst.* **1976**, *A32*, 751–767. [[CrossRef](#)]
37. Irshad, M.; Idrees, R.; Siraj, K.; Shakir, I.; Rafique, M.; Ain, Q.; Raza, R. Electrochemical Evaluation of Mixed Ionic Electronic Perovskite Cathode $\text{LaNi}_{1-x}\text{Co}_x\text{O}_{3-\delta}$ for IT-SOFC Synthesized by High Temperature Decomposition. *Int. J. Hydrogen Energy* **2021**, *46*, 10448–10456. [[CrossRef](#)]
38. Momma, K.; Izumi, F. VESTA 3 for Three-Dimensional Visualization of Crystal, Volumetric and Morphology Data. *J. Appl. Cryst.* **2011**, *44*, 1272–1276. [[CrossRef](#)]
39. Wei, W.; Chen, W.; Ivey, D.G. Rock Salt-Spinel Structural Transformation in Anodically Electrodeposited Mn-Co-O Nanocrystals. *Chem. Mater.* **2008**, *20*, 1941–1947. [[CrossRef](#)]
40. Chen, Z.; Wang, J.; Chao, D.; Baikie, T.; Bai, L.; Chen, S.; Zhao, Y.; Sum, T.C.; Lin, J.; Shen, Z. Hierarchical Porous $\text{LiNi}_{1/3}\text{Co}_{1/3}\text{Mn}_{1/3}\text{O}_2$ Nano-/Micro Spherical Cathode Material: Minimized Cation Mixing and Improved Li^+ Mobility for Enhanced Electrochemical Performance. *Sci. Rep.* **2016**, *6*, 25771. [[CrossRef](#)]
41. Gao, X.; Ashok, J.; Kawi, S.; Yang, N. Steam Reforming of Toluene as Model Compound of Biomass Tar over Ni-Co/ La_2O_3 Nano-Catalysts: Synergy of Ni and Co. *Int. J. Hydrogen Energy* **2021**, *46*, 30926–30936. [[CrossRef](#)]
42. Monaco, L.; Sodhi, R.N.S.; Palumbo, G.; Erb, U. XPS Study on the Passivity of Coarse-Grained Polycrystalline and Electrodeposited Nanocrystalline Nickel-Iron (NiFe) Alloys. *Corros. Sci.* **2020**, *176*, 108902. [[CrossRef](#)]
43. Latsiou, A.; Lykos, C.; Bairamis, F.; Konstantinou, I. Synthesis and characterization of $\text{LaCo}_x\text{Ni}_{1-x}\text{O}_3$ perovskites as heterogeneous catalysts for phenolics degradation by persulfate activation. *J. Chem. Technol. Biotechnol.* **2022**, *97*, 3467–3480. [[CrossRef](#)]
44. Wei, G.; Zheng, D.; Xu, L.; Guo, Q.; Hu, J.; Sha, N.; Zhao, Z. Photothermal catalytic activity and mechanism of $\text{LaNi}_x\text{Co}_{1-x}\text{O}_3$ ($0 \leq x \leq 1$) perovskites for CO_2 reduction to CH_4 and CH_3OH with H_2O . *Mater. Res. Express* **2019**, *6*, 086221. [[CrossRef](#)]
45. Dalpian, G.M.; Zhao, X.G.; Kazmerski, L.; Zunger, A. Formation and Composition-Dependent Properties of Alloys of Cubic Halide Perovskites. *Chem. Mater.* **2019**, *31*, 2497–2506. [[CrossRef](#)]
46. Hu, Z.; Lin, Z.; Su, J.; Zhang, J.; Chang, J.; Hao, Y. A Review on Energy Band-Gap Engineering for Perovskite Photovoltaics. *Solar RRL* **2019**, *3*, 1900304. [[CrossRef](#)]
47. Zarrin, N.; Husain, S.; Khan, W.; Manzoor, S. Sol-Gel Derived Cobalt Doped LaCrO_3 : Structure and Physical Properties. *J. Alloys Compd.* **2019**, *784*, 541–555. [[CrossRef](#)]
48. Qiao, L.; Zhang, S.; Xiao, H.Y.; Singh, D.J.; Zhang, K.H.L.; Liu, Z.J.; Zu, X.T.; Li, S. Orbital Controlled Band Gap Engineering of Tetragonal BiFeO_3 for Optoelectronic Applications. *J. Mater. Chem. C Mater.* **2018**, *6*, 1239–1247. [[CrossRef](#)]
49. Singh, C.; Rakesh, M. Preparation and Characterization of Nickel Doped, A and B Site LaCoO_3 Perovskite. *Indian J. Eng. Mater. Sci.* **2009**, *16*, 288–290.
50. Aswin, V.; Kumar, P.; Singh, P.; Gupta, A.; Rayaprol, S.; Dogra, A. Influence of Al Doping in LaCoO_3 on Structural, Electrical and Magnetic Properties. *J. Mater. Sci.* **2014**, *50*, 366–373. [[CrossRef](#)]
51. Luo, Y.; Wang, X.; Qian, Q.; Chen, Q. Studies on B Sites in Fe-Doped LaNiO_3 Perovskite for SCR of NO_x with H_2 . *Int. J. Hydrogen Energy* **2014**, *39*, 15836–15843. [[CrossRef](#)]
52. Ma, F.; Chu, W.; Huang, L.; Yu, X.; Wu, Y. Steam Reforming of Ethanol over Zn-Doped LaCoO_3 Perovskite Nanocatalysts. *Chin. J. Catal.* **2011**, *32*, 970–977. [[CrossRef](#)]
53. Zhou, C.; Liu, X.; Wu, C.; Wen, Y.; Xue, Y.; Chen, R.; Zhang, Z.; Shan, B.; Yin, H.; Wang, W.G. NO Oxidation Catalysis on Copper Doped Hexagonal Phase LaCoO_3 : A Combined Experimental and Theoretical Study. *Phys. Chem. Chem. Phys.* **2014**, *16*, 5106–5112. [[CrossRef](#)]
54. Mahmoodi, N.M. Binary Catalyst System Dye Degradation Using Photocatalysis. *Fibers Polym.* **2014**, *15*, 273–280. [[CrossRef](#)]
55. Maurya, N.S.; Mittal, A.K.; Cornel, P.; Rother, E. Biosorption of Dyes Using Dead Macro Fungi: Effect of Dye Structure, Ionic Strength and pH. *Bioresour. Technol.* **2006**, *97*, 512–521. [[CrossRef](#)] [[PubMed](#)]
56. Yu, K.; Yang, S.; He, H.; Sun, C.; Gu, C.; Ju, Y. Visible Light-Driven Photocatalytic Degradation of Rhodamine B over NaBiO_3 : Pathways and Mechanism. *J. Phys. Chem. A* **2009**, *113*, 10024–10032. [[CrossRef](#)]

57. Horikoshi, S.; Saitou, A.; Hidaka, H. Environmental Remediation by an Integrated Microwave/UV Illumination Method. V. Thermal and Nonthermal Effects of Microwave Radiation on the Photocatalyst and on the Photodegradation of Rhodamine-B under UV/Vis Radiation. *Environ. Sci. Technol.* **2003**, *37*, 5813–5822. [[CrossRef](#)]
58. Yao, S.; Wu, J.; Li, W.; Zheng, R.; Li, R.; Chen, Y.; Luo, J.; Zhou, X. LaCoO₃ Co-Catalyst Modified Ag₂CrO₄ for Improved Visible-Light-Driven Photocatalytic Degradation of Tetracycline. *Sep. Purif. Technol.* **2019**, *227*, 115691. [[CrossRef](#)]
59. Zhong, S.; Sun, Y.; Xin, H.; Yang, C.; Chen, L.; Li, X. NO Oxidation over Ni–Co Perovskite Catalysts. *Chem. Eng. J.* **2015**, *275*, 351–356. [[CrossRef](#)]
60. Salman, A.R.; Hyrve, S.M.; Regli, S.K.; Zubair, M.; Enger, B.C.; Lødeng, R.; Waller, D.; Rønning, M. Catalytic Oxidation of NO over LaCo_{1-x}B_xO₃ (B=Mn, Ni) Perovskites for Nitric Acid Production. *Catalysts* **2019**, *9*, 429. [[CrossRef](#)]
61. Qi, S.; Zhang, W.; Li, X.; Wang, Q.; Zhu, Z.; Zhou, T.; Wang, G.; Xie, A.; Luo, S. Catalytic Oxidation of Toluene over B-site Doped La-based Perovskite LaNi_xB_{1-x}O₃ (B=Co, Cu) Catalysts. *Env. Prog. Sustain. Energy* **2022**, *42*, e13965. [[CrossRef](#)]
62. Manos, D.; Papadopoulou, F.; Margellou, A.; Petrakis, D.; Konstantinou, I. Heterogeneous Activation of Persulfate by LaMO₃ (M=Co, Fe, Cu, Mn, Ni) Perovskite Catalysts for the Degradation of Organic Compounds. *Catalysts* **2022**, *12*, 187. [[CrossRef](#)]
63. Fabbri, E.; Nachttegaal, M.; Binninger, T.; Cheng, X.; Kim, B.J.; Durst, J.; Bozza, F.; Graule, T.; Schäublin, R.; Wiles, L.; et al. Dynamic Surface Self-Reconstruction Is the Key of Highly Active Perovskite Nano-Electrocatalysts for Water Splitting. *Nat. Mater.* **2017**, *16*, 925–931. [[CrossRef](#)] [[PubMed](#)]
64. Chen, Y.; Sun, Y.; Wang, M.; Wang, J.; Li, H.; Xi, S.; Wei, C.; Xi, P.; Sterbinsky, G.E.; Freeland, J.W.; et al. Lattice Site-Dependent Metal Leaching in Perovskites toward a Honeycomb-like Water Oxidation Catalyst. *Sci. Adv.* **2021**, *7*, 1788. [[CrossRef](#)]
65. Tummino, M.L.; Laurenti, E.; Deganello, F.; Bianco Prevot, A.; Magnacca, G. Revisiting the Catalytic Activity of a Doped SrFeO₃ for Water Pollutants Removal: Effect of Light and Temperature. *Appl. Catal. B* **2017**, *207*, 174–181. [[CrossRef](#)]
66. Sun, X.; Lin, J. Synergetic Effects of Thermal and Photo-Catalysis in Purification of Dye Water over SrTi_{1-x}Mn_xO₃ Solid Solutions. *J. Phys. Chem. C* **2009**, *113*, 4970–4975. [[CrossRef](#)]
67. Wiranwetchayan, O.; Promnopas, S.; Phadungdhitidhada, S.; Phuruangrat, A.; Thongtem, T.; Singjai, P.; Thongtem, S. Characterization of Perovskite LaFeO₃ Synthesized by Microwave Plasma Method for Photocatalytic Applications. *Ceram. Int.* **2019**, *45*, 4802–4809. [[CrossRef](#)]
68. Lim, T.H.; Cho, S.J.; Yang, H.S.; Engelhard, M.H.; Kim, D.H. Effect of Co/Ni Ratios in Cobalt Nickel Mixed Oxide Catalysts on Methane Combustion. *Appl. Catal. A Gen.* **2015**, *505*, 62–69. [[CrossRef](#)]
69. Zafeiratos, S.; Dintzer, T.; Teschner, D.; Blume, R.; Hävecker, M.; Knop-Gericke, A.; Schlögl, R. Methanol Oxidation over Model Cobalt Catalysts: Influence of the Cobalt Oxidation State on the Reactivity. *J. Catal.* **2010**, *269*, 309–317. [[CrossRef](#)]
70. Zhong, L.; Kropp, T.; Baaziz, W.; Ersen, O.; Teschner, D.; Schlögl, R.; Mavrikakis, M.; Zafeiratos, S. Correlation between Reactivity and Oxidation State of Cobalt Oxide Catalysts for CO Preferential Oxidation. *ACS Catal.* **2019**, *9*, 8325–8336. [[CrossRef](#)]
71. Toby, B.H.; von Dreele, R.B. GSAS-II: The Genesis of a Modern Open-Source All Purpose Crystallography Software Package. *J. Appl. Crystallogr.* **2013**, *46*, 544–549. [[CrossRef](#)]
72. Brunauer, S.; Emmett, P.H.; Teller, E. Adsorption of Gases in Multimolecular Layers. *J. Am. Chem. Soc.* **1938**, *60*, 309–319. [[CrossRef](#)]
73. Barrett, E.P.; Joyner, L.G.; Halenda, P.P. The Determination of Pore Volume and Area Distributions in Porous Substances. I. Computations from Nitrogen Isotherms. *J. Am. Chem. Soc.* **1951**, *73*, 373–380. [[CrossRef](#)]

Disclaimer/Publisher’s Note: The statements, opinions and data contained in all publications are solely those of the individual author(s) and contributor(s) and not of MDPI and/or the editor(s). MDPI and/or the editor(s) disclaim responsibility for any injury to people or property resulting from any ideas, methods, instructions or products referred to in the content.